

Phase Transitions

Chiral Bent-Shaped Molecules Exhibiting Unusually Wide Range of Blue Liquid-Crystalline Phases and Multistimuli-Responsive Behavior

Vidhika Punjani,^[a] Golam Mohiuddin,^[a] Supreet Kaur,^[a] Angshuman Roy Choudhury,^[a] Sathyanarayana Paladugu,^[b] Surajit Dhara,^[b] Sharmistha Ghosh,^[c] and Santanu Kumar Pal^{*(a)}

Abstract: Recently, an unprecedented observation of polar order, thermochromic behavior, and exotic mesophases in new chiral, bent-shaped systems with a $-\text{CH}_3$ moiety placed at the transverse position of the central core was reported. Herein, a homologous series of compounds with even-numbered carbon chains from $n=4$ to 18 were synthesized, in which $-\text{Cl}$ was substituted for $-\text{CH}_3$ at the kink position and a drastic modification in the phase structure of the bent-shaped molecule was observed. An unusual stabilization of the cubic blue phase (BP) over a wide range of 16.4°C has been witnessed. Two homologues in this series (1-12 and 1-14) exhibit an interesting phase sequence consisting of BPI/II, chiral nematic, twist grain boundary, smectic A, and smectic X (SmX) phases. The higher homologues (1-16 and 1-18) stabilize the SmX phase enantiotropically over the entire temperature range. Crystal structure analysis confirmed the

bent molecular architecture, with a bent angle of 148° , and revealed the presence of two different molecular conformations in an asymmetric unit of compound 1-4. A DFT study corroborated that the $-\text{Cl}$ moiety at the central core of the molecule led to an increase in the dipole moment along the transverse direction, which, in turn, facilitated the unusual stabilization of frustrated structures. Crystal polymorphism has been evidenced in three homologues (1-10, 1-12, and 1-14) of the series. On the application of mechanical pressure through grinding, compound 1-10 transformed from a bright yellow crystalline solid to a dark orange-green amorphous solid, which reversed upon dropwise addition of dichloromethane, indicating reversible mechanochromism in this class of compounds. In addition, excellent thermochromic behavior has been observed for compound 1-10 with a controlled temperature-color combination.

Introduction

Chirality is ubiquitous in nature and is accountable for the development of living and nonliving matter. Concurrently, it is immensely important for the pharmaceutical industry and for the propagation of contemporary technological advancement.^[1,2] The presence of the chiral center in a molecule can result in complex configurations. For example, if chirality is incorporated into a liquid-crystal (LC) system, it can produce complex phase structures, such as BPs (BPIII, BP II, BPI), twist grain boundary (TGB), smectic blue phase (SmBP), and chiral nematic (N*). The N* phase or a cholesteric liquid crystal (CLC)

is a twisted helicoidal state^[2] of the nematic phase. These chirality-induced phases find various applications in imaging devices, information displays, reflectors/polarizers, tunable band-pass filters, and temperature or pressure sensors.^[3-5] Compared with chiral liquids, LC materials, due to their ordered nature, along with liquidity, can amplify the molecular chirality by manifold.^[6,7] BP is a frustrated phase, consisting of double-twist cylinders, that occurs just below the isotropic liquid over a narrow temperature range.^[8-10] BPs are extremely important for the development of next-generation optoelectronic devices that do not require alignment layers (i.e., polyimide coating), which simplifies the LC display manufacturing process. They can also be used to develop devices such as light filters, lasers, fast light modulators, and tunable photonic crystals.^[11-13] The TGB phase, which is the LC analogue of the Abrikosov vortex state in "type II superconductors",^[14] is a rich, complex, and frustrated phase structure. It usually appears in the temperature range between the N* and Sm phases (SmA/A* or SmC*^{).}^[14-21]

In the contemporary era of LC research, bent-core liquid crystals (BCLCs) are the frontrunner, due to their extremely rich, diverse, and unparalleled phase structures.^[22] The presence of the small kink at the molecular core of the BCLC helps to develop additional order (unlike rodlike or disklike LCs) that

[a] V. Punjani, Dr. G. Mohiuddin, S. Kaur, Dr. A. R. Choudhury, Dr. S. K. Pal
Department of Chemical Sciences
Indian Institute of Science Education and Research (IISER) Mohali
Sector 81, Knowledge City, Manauli, 140306 (India)
E-mail: skpal@iisermohali.ac.in

[b] Dr. S. Paladugu, Dr. S. Dhara
School of Physics, University of Hyderabad, Hyderabad, 500046 (India)

[c] Dr. S. Ghosh
Department of Physics, University of Calcutta
92 Acharyya Prafulla Chandra Road, Kolkata, 700009 (India)

Supporting information and the ORCID identification number(s) for the author(s) of this article can be found under:
<https://doi.org/10.1002/chem.201905707>.

can be polar, biaxial nematic, octupolar, and/or chiral, despite being formed from achiral molecules.^[22–31] BCLCs, due to their negative bend-splay elastic constant ratio, if doped with an external chiral agent, can stabilize the frustrated BPs in the mixture,^[32] but single-component BCLCs exhibiting BPs and TGB phases are limited.^[33–38] A combination of the additional order of bent-core molecules with molecular chirality provided by the stereocenters present in the chiral moiety can lead to the stabilization of the frustrated phases.

There has been increasing interest in recent years in materials that have the ability to change their color, either reversibly or permanently, in response to applied external stimuli.^[39–42] Materials that exhibit a change in the photoluminescence properties upon application of mechanical pressure, grinding, shearing, or crushing are known as mechanochromic luminescent materials or piezochromic luminescent materials. These mechanochromic materials have potential applications in memory storage, sensors, security inks, pressure sensing, and optical-recording systems.^[39–42] The change in emission properties after grinding can be reversed by either solvent or thermal annealing. The reversibility of the neat compound is because there is no involvement of bond breakage, but there is a transformation of stacking modes involving weak interactions. BCLCs containing a salicylideneaniline moiety and cholesterol unit can be potentially used as mechanochromic materials. The salicylideneaniline moiety exhibits excited-state intramolecular proton transfer (ESIPT) due to the formation of intramolecular hydrogen bonding between –OH and –CH=N– and switches between the ESIPT ON/OFF state due to mechanical grinding. The cholesterol unit has the tendency to change color and circular dichroism with a change in the helical pitch and handedness.^[43–45] Therefore, the salicylideneaniline and cholesterol units play an important role in the mechanochromic behavior of this class of compounds.^[43–46] In our previous report,^[47] we showed that 3-amino-2-methylbenzoic acid (as the central core,^[47–49,52,53,55] Figure 1a) based smart bent-core materials exhibited frustrated structures that stabilized BPs for about 2.0 °C and the TGB phase for about 31.0 °C. The direct attachment of the cholesterol moiety to the central core, functioning as an

arm of the BCLC (Figure 1), promotes rigidity in the molecular architecture, which eventually leads to the realization of different frustrated phases. The methyl group (–CH₃), with the +I effect and its bulky size (relative to H), widened the bent angle and supported the stabilization of different phase structures. Unlike the methyl group (–CH₃), herein, we have purposely placed an electronegative chloro moiety (3-amino-2-chlorobenzoic acid as the central core^[50,51]) at the transverse position of the central core to realize its electronegative effect upon the stabilization of frustrated phases (Figure 1b). On one side of the core, there is a cholesterol moiety attached through an ester linkage, whereas, on the other side, there is a 4-*n*-alkoxy-2-hydroxybenzaldehyde moiety attached through an imine linkage. The homologous series with even chains, from *n*=4 to 18, was synthesized. An increase in the alkyl chain length leads to the thermodynamic stabilization of the liquid-crystalline material enantiotropically, as the series makes a transition from nonliquid crystalline (1-4, 1-6) to monotropic LC (1-8, 1-10, 1-12, and 1-14) and enantiotropic LC (1-16, 1-18). Compound 1-10 exhibited a stable BP over a wide range of 16.4 °C. In addition, we observe a variety of phases, such as BPI/II, N*, TGBA, SmA, and an unknown tilted phase, SmX, for two homologues (1-12 and 1-14), similar to that previously reported.^[47] Compounds 1-16 and 1-18 stabilize the SmX phase enantiotropically. The phase sequence of all compounds is summarized in Figure S83 in the Supporting Information during cooling. The presence of the –Cl moiety in the central core, which is evident from the single-crystal structure and density functional theory (DFT) analysis, has allowed more insights regarding stabilization of the frustrated structures in these molecular systems. Three of the compounds (1-10, 1-12, and 1-14) were shown to exhibit crystal polymorphism. An excellent thermochromic property has been observed for 1-10 with a controlled temperature–color combination. Application of a grinding force on 1-10 converted the yellow color of the sample to a dark orange–green color that can be reversed back to yellow color after the dropwise addition of a solvent (dichloromethane).

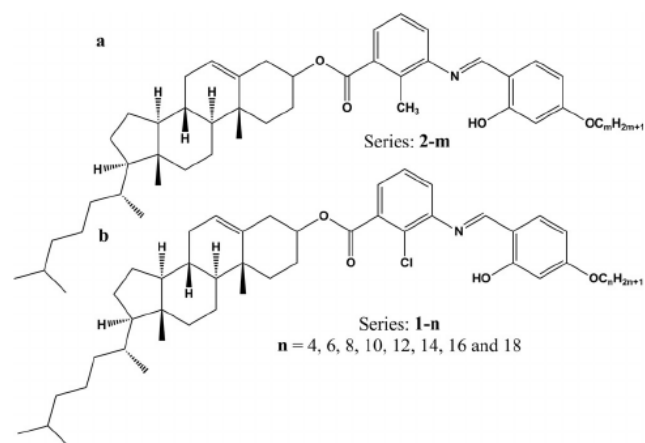


Figure 1. Chiral bent-core molecules with a) a –CH₃ moiety at the kink position (previously reported in ref. [47]) and b) a –Cl moiety at the kink position of the central unit (the molecule described herein).

Results and Discussion

Synthesis and characterization

Details of the synthetic approach are summarized in Scheme S1 in the Supporting Information, and the corresponding molecular characterizations are elaborated in Figures S1–S32 in the Supporting Information.

Single-crystal X-ray diffraction (SCXRD) studies

Interestingly, we were able to successfully grow crystals suitable for SCXRD experiments (see the Supporting Information for details) of one of the representative examples, compound 1-4, to demonstrate the bent angle of the compound, which is an important parameter in the field of BCLCs and investigate the elusive characteristics of molecular packing (Figure 2a–f).^[52–57] Compound 1-4 was found to crystallize in the monoclinic

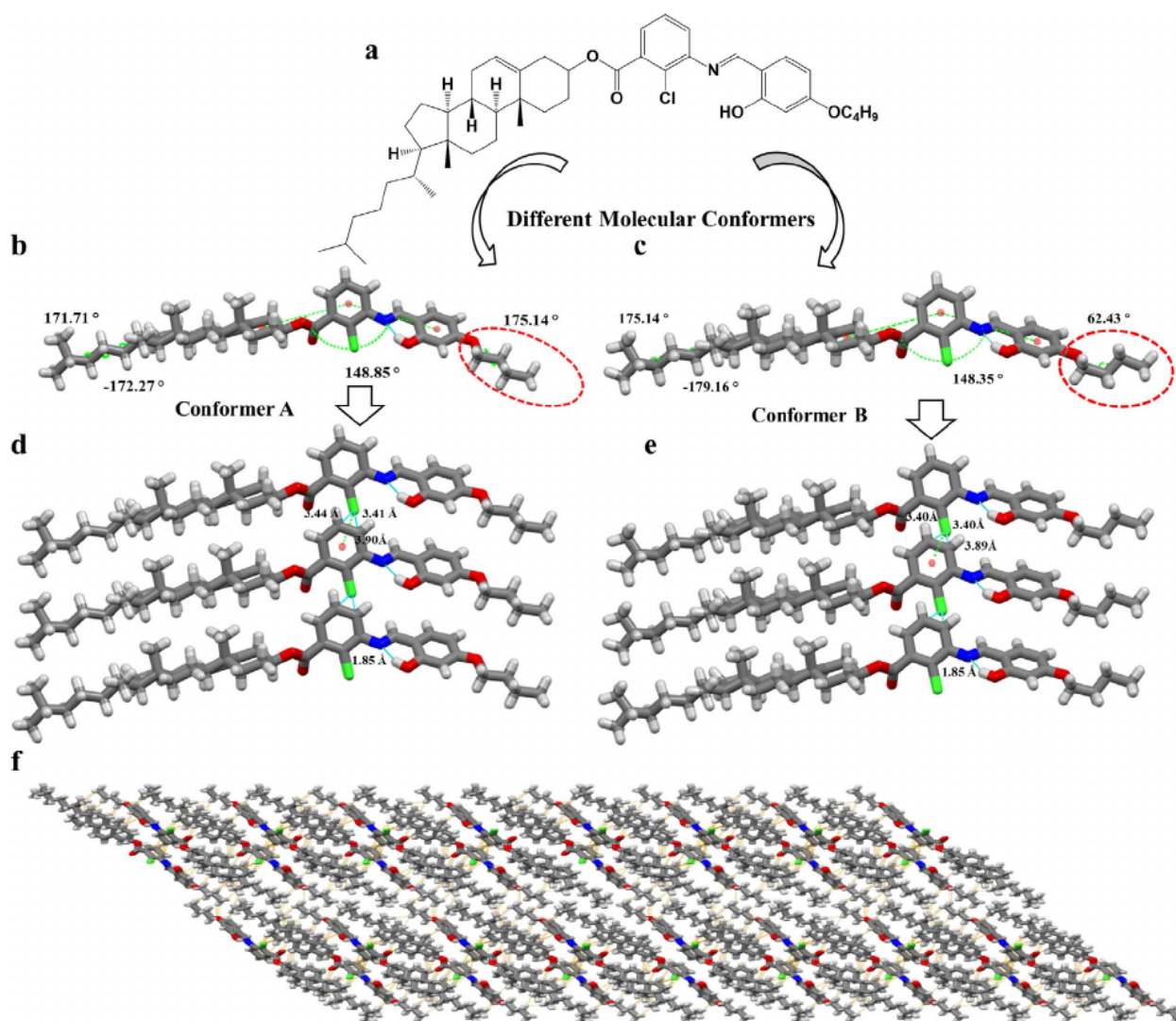


Figure 2. a) Structure of the lowest homologue. Molecular crystal structure of b) conformers A (1-4) and c) B (1-4) with dihedral angles varying at the terminal alkyl chain and cholesterol moiety. d) Conformer A (1-4) with C–Cl \cdots π interactions and e) conformer B (1-4) with C–Cl \cdots π interactions. f) The 3D structural arrangement of 1-4.

system with the $P2_1$ space group, with two independent molecules of different conformations (conformations A (C1A to C45A) and B (C1B to C45B)) in the asymmetric unit ($Z=4$, $Z'=2$). Structural analysis revealed the major dissimilarities in these two conformations at the terminal $-\text{OC}_4\text{H}_9$ chain and in the alkyl chain of the cholesterol moiety (Figure 2b,c). C1A–C2A–C3A–C4A in conformer A ($\angle\text{C2A–C3A–C4A–O1A}=175.14(7)^\circ$) adopted an *anti* conformation with respect to the C3A–C4A bond, (Figure 2b), whereas C1B–C2B–C3B–C4B in conformer B ($\angle\text{C2B–C3B–C4B–O1B}=62.43(11)^\circ$) adopted a staggered conformation with respect to the C3B–C4B bond (Figure 2c). Another significant difference in the conformations was observed in the alkyl chain of the cholesterol moiety ($\angle\text{C35A–C38A–C40A–C41A}=172.27(6)^\circ$ and $\angle\text{C40A–C41A–C42A–C43A}=171.71(8)^\circ$ in conformer A (Figure 2b); $\angle\text{C35B–C38B–C40B–C41B}=-179.16(7)^\circ$ and $\angle\text{C40B–C41B–C42B–C43B}=175.14(8)^\circ$ in conformer B (Figure 2c)).

Most importantly, the molecule attained a bent-shaped geometry with a bent angle (the angle between the centroids of the rings C5A–C6A–C7A–C8A–C9A–C10A, C12A–C13A–C14A–C15A–C16A–C17A, and C19A–C20A–C21A–C22A–C23A–C24A of conformer A and C5B–C6B–C7B–C8B–C9B–C10B, C12B–C13B–C14B–C15B–C16B–C17B, and C19B–C20B–C21B–C22B–C23B–C24B of conformer B) of 148.85° for conformer A (Figure 2b) and 148.35° for conformer B (Figure 2c). Details of the structural analysis are summarized in Figures S33–S39 and Tables S1–S4 in the Supporting Information. Other than these major differences, the two molecules had differences in other bond angles and torsion angles of $\pm 2^\circ$. These differences were manifested by $Z'=2$ with a large unit cell ($V=4046.7(4) \text{ \AA}^3$; Table S5 in the Supporting Information). The structure of the cholesterol-based BC compound under investigation is shown in Figure 2a, for which the bent architecture was proved by means of SCXRD analysis.

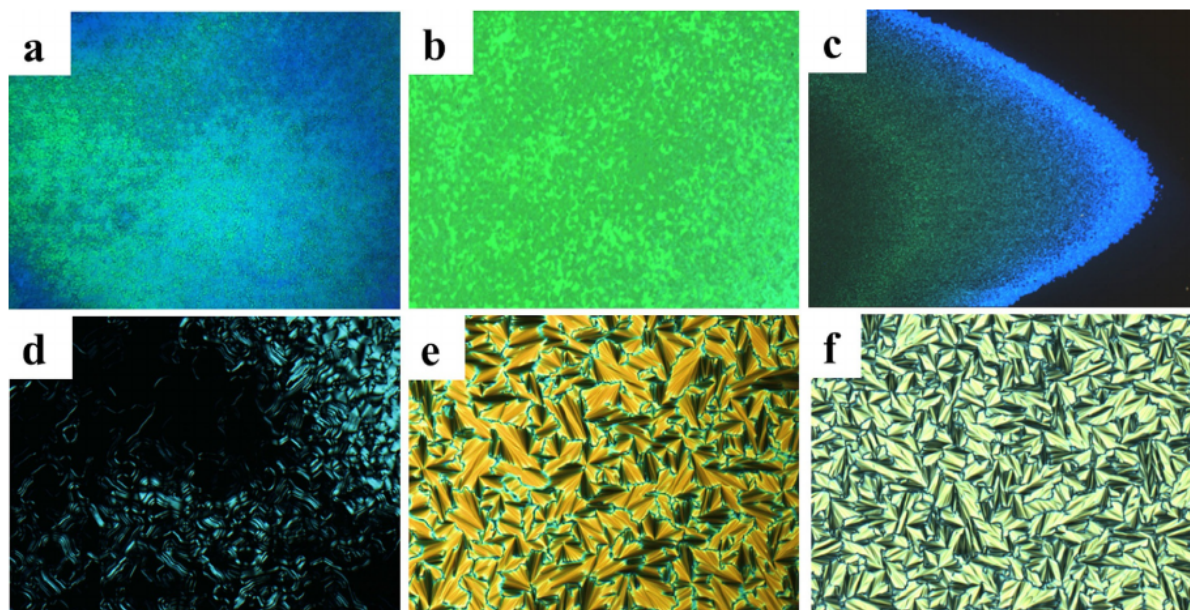


Figure 3. POM micrographs of BPI (a) and BPII (b) phases of compound 1-10 at 121.5 and 118.0 °C, respectively, in a 4.8 μm polyimide-indium tin oxide (ITO)-coated planar cell; c) cubic BP of compound 1-10 at 126.8 °C on a normal glass coverslip; d) filamentous texture of the TGBA phase of compound 1-14 at 125.8 °C in a 3.3 μm polyimide-ITO-coated homeotropic cell; SmA (e) and SmX (f) phases of compound 1-12 at 113.8 and 105.2 °C, respectively, in a 4.8 μm polyimide-ITO-coated planar cell.

A DFT study was performed on compound 1-4 (as a representative case) and an analogous compound with a methyl core reported earlier.^[47] It was found that the dipole moment along the *y* direction (Figure S40 and Tables S6 and S7 in the Supporting Information) was much larger ($\mu_y = 2.55$ D) in compound 1-4 than that in the previously reported molecule ($\mu_y = 1.272$ D), although the dipole moments along the other two directions (*x* and *z*) remained similar in both compounds. This observation implies that the introduction of the $-Cl$ moiety in the kink direction of the molecule (Figure 2a) electronically affects nucleation of the usual mesophases (e.g., nematic or Sm) and stabilizes the frustrated BPs.

Thermal behavior: Polarized optical microscopy (POM) and differential scanning calorimetry (DSC) studies

The phase transition temperature of BPs was not observed by means of DSC, but rather a POM study in reflectance mode was employed to determine the BP range of the compounds. On a normal glass slide with a coverslip (without any coating), compound 1-10 (as a representative case) melted at a temperature of 145.4 °C, which, upon cooling (rate 0.5 °C min⁻¹), formed a striking platelet-like texture (Figure 3c) of cubic BP, appearing at a temperature of 129.0 °C and retained up to 125.2 °C. A further decrease in temperature from 125.2 °C led to the nucleation of the helical N_{cyb}^* phase, which crystallized at 105.6 °C. A surprising result was observed if compound 1-10 was used to fill a 4.8 μm polyimide-ITO-coated homogeneous/planar cell, which was investigated by means of POM. This sample exhibited the appearance of a platelet-like texture of cubic BPs at 124.9 °C, which remained stable up to 108.5 °C (cooling rate 0.5 °C min⁻¹; Figure 3a,b and Figure S47 in the Supporting Information). Hence, the BP range was extended

from 3.8 (Figure S45 in the Supporting Information; on a normal glass slide with a coverslip) to 16.4 °C (elaborated in Figure S47 in the Supporting Information), if inserted in a planar cell, which was also substantially stable (Figure S46 in the Supporting Information). Available literature suggests that this is a rare report of single-component BCLCs forming a cubic BP structure stabilized by a range of 16.4 °C. Upon further cooling the sample, the N_{cyb}^* phase appeared and crystallized at 100.6 °C. The above results were attained at a cooling rate of 0.5 °C min⁻¹. However, if the rate of cooling was 3 °C min⁻¹, crystallization was suppressed and attained at a temperature of 90.4 °C (Figure S48 in the Supporting Information). This observation of elongation of the BP range and suppression of crystallization was also reported earlier.^[58]

For compound 1-14, on a normal glass slide with a coverslip (without any coating), upon cooling, a transient BP (Figure S55 in the Supporting Information) was observed followed by the appearance of a focal conic-type texture of N^* at 128.4 °C, which, upon further cooling, changed to a fingerprint-like^[59] texture typical of the TGBA phase at 126.0 °C. The fingerprint texture further transformed into a characteristic filamentous^[59] texture of TGBA and started to become homeotropic at 121.4 °C (Figure S56 in the Supporting Information). Crystallization of 1-14 was observed at 78 °C. However, compound 1-14 (inserted in a 3.2 μm polyimide-ITO-coated planar cell) during cooling, exhibited the appearance of BP, N^* , and TGBA phases (Figure S58 in the Supporting Information). Upon further cooling, focal conic-like textures characteristic of SmA start to appear below the TGBA phase. Below the SmA phase, an unidentified tilted phase, SmX, forms at a temperature of 117.6 °C. The change of SmA to SmX is characterized by the development of stripes on focal conics (Figure S59 in the Supporting Information). Similarly, compound 1-14, if inserted in a

3.3 μm polyimide-ITO-coated homeotropic cell, confirmed the formation of the TGBA phase through a characteristic fingerprint and filamentous texture (Figure 3d and Figure S57 in the Supporting Information). Compound 1-12 exhibits a similar phase sequence of BPI/II, N*, TGBA, SmA, and SmX (Figures S49–S54 in the Supporting Information). POM micrographs of 1-12 for SmA and SmX are shown in Figure 3e and f, respectively. Compounds 1-16 and 1-18 showed enantiotropic mesomorphism and exhibited the SmX phase in the heating and cooling cycles. Details of the POM study of compounds 1-8, 1-14, and 1-18 are discussed in detail in Figures S43, S44, and S60–S68 in the Supporting Information. The observed mesophases, transition temperatures, and associated enthalpies, as observed by means of DSC, are summarized in Table 1 (Figures S69 and S70 in the Supporting Information).

Table 1. Phase transition temperatures (peak temperature, °C) and enthalpies of transition (ΔH [kJ mol⁻¹] in parentheses) determined by means of DSC (scan rate of 10 °C min⁻¹, second heating and cooling cycles) and POM.

Compound	Phase transitions ^[a]
1-4	heating: Cr 176.1 (20.2) Iso cooling: Iso 120.8 (6.4) Cr
1-6	heating: Cr 152.0 (20.5) Iso cooling: Iso 134.2 (20.1) Cr
1-8	heating: Cr 150.3 (29.9) Iso cooling: Iso 124.9 BPI/II ^[b] 115.2 Cr ^[b]
1-10	heating: Cr ₁ 110.0 (3.3) Cr ₂ 145.4 (21.2) Iso cooling: Iso 124.9 BPI/II ^[b] 108.5 N _{cyb} ^{*(b)} 100.6 Cr ₁ ^[b]
1-12	heating: Cr ₁ 132.8 (29.0) Iso cooling: Iso 131.5 BPI/II 128.9 (0.96) N* 125.0 TGBA 123.7 SmA ^[b] 111.0 SmX ^[b] 95 Cr ₂ 46.5 (2.5) Cr ₁
1-14	heating: Cr _{1a} 61.7 (8.0) Cr _{2b} 70.4 (24.3) Cr _{3c} 136.7 (46.8) Iso cooling: Iso 128.7 BPI/II 128.4 (3.6) N* 126.0 TGBA 121.4 SmA ^[b] 117.6 SmX ^[b] 78.0 Cr ₄ ^[c]
1-16	heating: Cr 116.9 (13.6) SmX 133.5 (4.8) Iso cooling: Iso 131.3 (4.8) SmX 94.4 (4.8) Cr
1-18	heating: Cr 113.7 (10.5) SmX 132.8 (4.1) Iso cooling: Iso 131.6 (4.2) SmX 97.6 (10.6) Cr

[a] Cr = crystal; Iso = isotropic; N_{cyb}^{*} = chiral nematic phase composed of Sm clusters; TGBA = twist grain boundary phase; Smectic A = SmA; Smectic X = SmX. [b] Phase transitions observed by means of POM in an ITO-coated planar cell (antiparallel rubbing). [c] Phase transitions observed by means of SAXS/WAXS. (1-14: Cr_{1a} = amorphous, Cr_{2b} = transition crystalline state, Cr_{3c} = crystal polymorph.)

Small- and wide-angle X-ray (SAXS/WAXS) studies

SAXS/WAXS analyses were carried out on LC samples in a 0.7 mm capillary to gain more insights into the LC phase behavior. The X-ray diffractogram of compound 1-10 at 115 °C showed two diffused peaks: one in the small-angle region, with a d value of 39.49 Å, and the other in the wide-angle region, with a d value of 5.78 Å (Figure 4a). This observation of diffuse peaks in both small- and wide-angle regions confirmed the presence of a disordered mesophase. In the XRD scan of 1-10 upon cooling, the intensity of the small-angle peak was greater than that of the wide-angle peak,^[60,61] indicating the presence of clusters in the chiral nematic phase (N_{cyb}^{*}; Figure 4a and Figure S71b in the Supporting Information). The in-

tensity of the small-angle peak became sharper with a gradual decrease in temperature, which also substantiated the earlier observation of cluster formation (as $d/L \approx 0.89$ – 0.96) in the N_{cyb}^{*} phase (Figure S71a in the Supporting Information). The correlation length (ξ) and d spacing for 1-10 increased with decreasing temperature over the entire nematic range, inferring the cybotactic nature of the chiral nematic phase (N_{cyb}^{*}; Figure 4c). The value of d spacing increased from 31.89 to 39.49 Å, whereas the correlation length increased from 55.30 to 446.35 Å as the sample was cooled from the melted liquid (Table S8 in the Supporting Information).

For compound 1-14, a transient chiral nematic (N*) phase was observed. The XRD profile of 1-14 at 128 °C was composed of two diffused peaks: one in the small-angle region, with a d value of 38.89 Å, and the other in the wide-angle region, with a d value of 5.73 Å, which confirmed the nematic phase (Figure 4b). A gradual decrease in temperature led to the formation of a sharper and more intense small-angle peak, showing nucleation of N*, TGBA, SmA, and SmX phases from the isotropic melt, whereas the wide-angle peak remained diffuse, as observed earlier (Figure S75a in the Supporting Information). Upon cooling to 80 °C, the XRD results for compound 1-14 consisted of a sharp small-angle peak with a d value of 35.54 Å and a wide-angle halo with a d value of 5.61 Å (Figure 4b). The $d=f(T)$ plot analysis showed that, at first, the d value increased from 34.49 to 42.83 Å up to 125 °C and further decreased from 42.83 to 35.54 Å until the compound crystallized at 78 °C. This proved the exhibition of TGBA, SmA, and SmX phases (Figure 4d and Table S10 and Figure S80 in the Supporting Information), in which $d/L \approx 0.95$ for TGBA, $d/L \approx 0.94$ for SmA, and d/L decreased with temperature from 0.92 to 0.79 for SmX. The plot of $\xi=f(T)$ displayed a drastic increase in the correlation length as the sample made a transition from N* to TGBA from 58.34 to 956.71 Å, which further increased after 956.71 Å to 1520.89 Å (Figure 4d, Table S10 in the Supporting Information). XRD analyses of 1-12, 1-14, 1-16, and 1-18 are discussed in detail in Figures S73, S75b, S76–S79, S81, and S82 and Tables S9 and S11 in the Supporting Information.

Dielectric measurements

We performed dielectric relaxation studies on compound 1-18 as a representative example of the SmX phase. Compound 1-18 was used to fill a planar cell made of two ITO-coated glass plates with a separation of 8 μm . Both real and imaginary parts of the dielectric constants were measured in the frequency range of 1 kHz to 1 MHz at various temperatures. Compound 1-18 exhibited dielectric relaxation throughout the entire SmX phase and frequency dispersions of real and imaginary parts of dielectric constants at 120, 117, and 112 °C are presented in Figure 5a–c. It should be noted from Figure 5 that 1-18 exhibited two relaxations: one at a low frequency, which was temperature dependent, and the other at high frequency (≈ 1 MHz), which was temperature independent. The low-frequency dielectric relaxation was due to the molecular dipoles and the high-frequency relaxation due to the finite resistance of the ITO layers. The relaxations were fitted with a complex di-

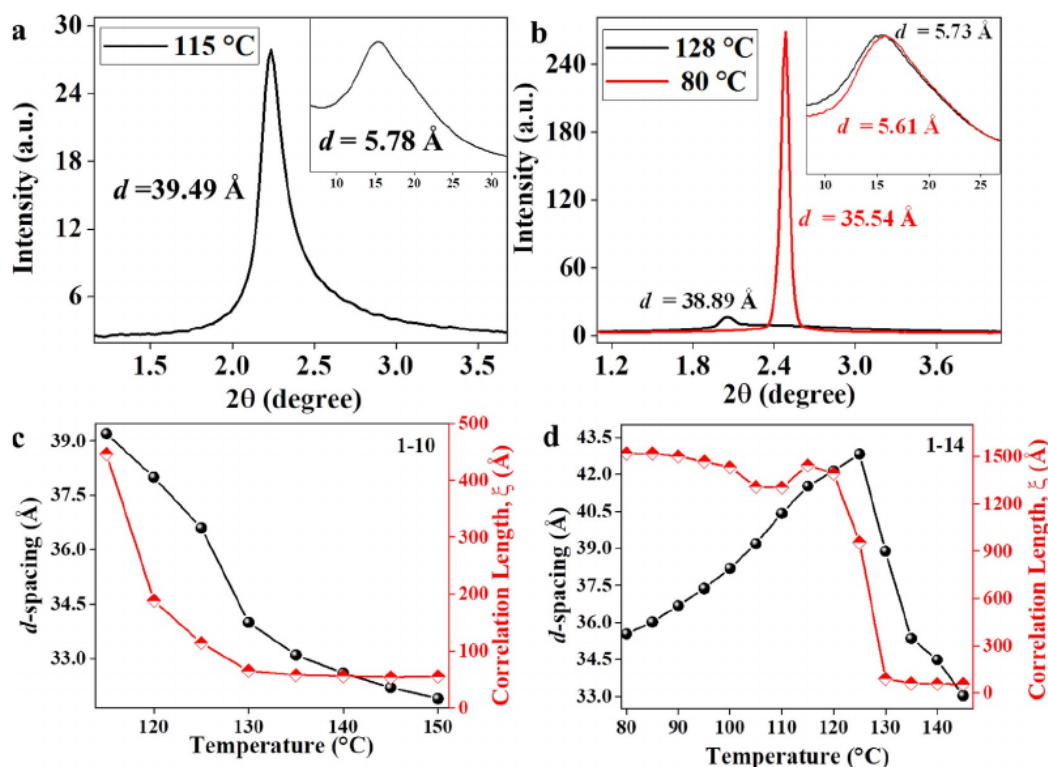


Figure 4. Intensity versus 2θ plot showing a) the N_{cyb}^* phase of compound 1-10 in the small-angle region; inset showing the wide-angle peaks, b) the N^* and SmX phases of compound 1-14 in the small-angle region; inset showing the wide-angle peaks. Plot of d spacing and correlation length (small-angle peak) versus temperature for compounds 1-10 (c) and 1-14 (d).

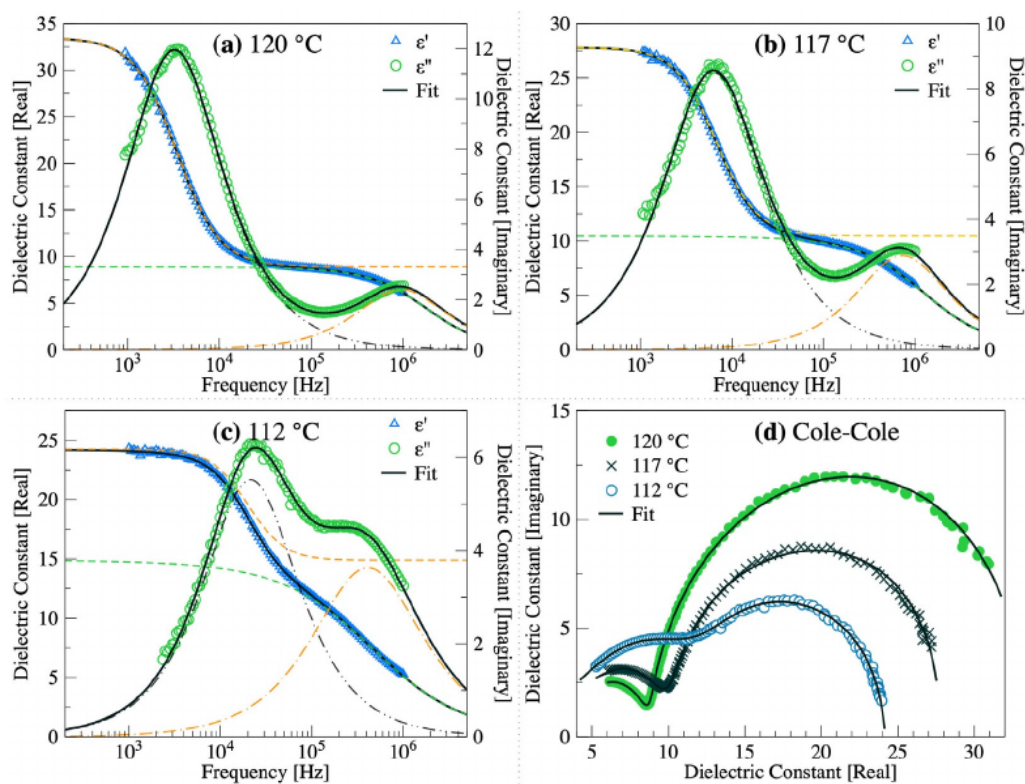


Figure 5. Frequency dispersions of real (triangles) and imaginary (circles) parts of dielectric constants at a) 120, b) 117, and c) 112 °C of 1-18. d) Cole–Cole plot of 1-18.

electric constant ($\epsilon^* = \epsilon' - i\epsilon''$) as a function of frequency to obtain the dipole relaxation frequency. The complex dielectric constant is given by Equation (1):^[62]

$$\epsilon^* = \epsilon' - i\epsilon'' = \frac{\epsilon_0 - \epsilon_1}{(1 + i\omega\tau)^{1-\alpha}} + \frac{\epsilon_1 - \epsilon_\infty}{(1 + i\omega\tau_1)^{1-\alpha}} + \epsilon_\infty \quad (1)$$

in which ϵ_0 is the static dielectric permittivity, ϵ_∞ is the high-frequency limit of the dielectric constant, α and α_1 are the Cole–Cole distribution parameters, and τ and τ_1 are the relaxation times of low and high relaxation modes. The fits of complex dielectric constant are shown in Figure 5 with continuous lines. The values of α and α_1 were found to be very small (< 0.02), which suggested that the relaxation was of Debye type, and this was further supported by Cole–Cole plots (Figure 5d).

The temperature-dependent relaxation time, as a function of $1/T$, is shown in Figure 6. Below the isotropic transition, the relaxation time (τ) decreases slowly at the beginning (region I) and then decreases rapidly in the middle of the SmX phase (region II). As the temperature approaches the crystalline phase, the relaxation time again decreases very slowly with a different slope (region III). This trend is opposite to that of typical Arrhenius behavior. However, such anomalous behavior was observed in several liquid-crystalline systems and often attributed to supramolecular LC formation.^[63–65] As far as the uncommon temperature dependence of the dielectric relaxation times is concerned, this is probably due to an additional polar ester linking group, which causes a larger dipole moment, and their

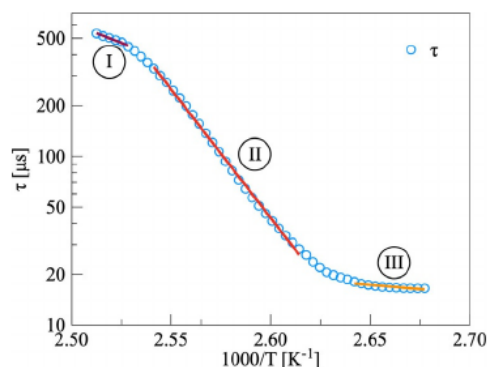


Figure 6. Variation of relaxation time (semilogarithmic scale) as a function of $1/T$ in the SmX phase of compound 1-18. The continuous line is a theoretical fit to the Arrhenius equation.

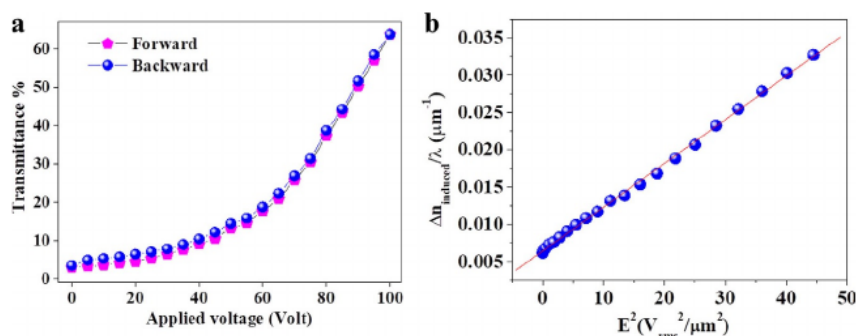


Figure 7. a) Voltage versus transmission curve for 1-10 at $T - T_{\text{iso-BP}} = -2$ °C. b) Plot of $\Delta n_{\text{induced}}/\lambda$ as a function of E^2 .

repulsive interaction accounts for an increase in relaxation time with increasing temperature.^[66]

To obtain a quantitative estimation, three different regions of the curve are fitted to the Arrhenius equation, $\tau = \tau_0 \exp(U/RT)$, in which U is the activation energy (shown in Figure 6 with a continuous line). It gives negative activation energies: values of 88, 292, and 20 kJ mol^{-1} in regions I, II, and III, respectively. These results suggest that the relaxation mechanisms in the SmX phase are very complex.

The higher values of activation energy could be due to the enhanced elasticity and soft-glassy behavior of the SmX phase.^[67] The dielectric study of compound 1-10 is elaborated in Figure S84 in the Supporting Information.

Electro-optical (EO) performance

A typical voltage versus transmission (V - T) curve in the BP of compound 1-10 is shown in Figure 7a. The in-plane switching (IPS)-type cell (Instec USA), with comb-type interdigitated electrodes fabricated on the bottom substrate, was used for the EO study. The width of the electrodes and the distance between them were both 15 μm . The cell gap was 9 μm . The substrates had homogeneous alignment and rubbing was done parallel to the electrode, although no surface treatment was necessary for the BP. Transmission gradually increased with applied voltage; however, only 65% transmission was observed at a maximum applied voltage (≈ 100 V). Upon decreasing the voltage, V - T almost overlapped with that of the increased voltage and only a slight hysteresis was observed. However, this hysteresis-free behavior was obtained up to 2 °C below the isotropic to BP transition temperature ($T_{\text{iso-BP}}$). Beyond this temperature range, the electric-field-induced transition from BP to N^* was observed. As the strength of the electric field increased, the medium became anisotropic along the electric-field direction and the change in birefringence obeyed the Kerr effect in the low-field region. The output light intensity (I_{out}) is given by $I_{\text{out}} = I_{\text{in}} \sin^2(\phi/2)$, in which I_{in} is the input intensity and ϕ is the optical retardation. The induced birefringence, $\Delta n_{\text{induced}}$, can be obtained from $\phi = 2\pi d \Delta n_{\text{induced}}/\lambda$, in which d is the cell gap and λ is the wavelength of the incident light. Because the ratio of induced birefringence to the wavelength of the incident light in the low-field region is proportional to the square of the electric field and the proportionality

constant is the Kerr constant (K) of the medium, $\Delta n_{\text{induced}}/\lambda = KE^2$ (E = electric field). Figure 7b shows the plot for $\Delta n_{\text{induced}}/\lambda$ versus the square of the electric field (E^2) at $T - T_{\text{iso-BP}} = -2^\circ\text{C}$. Within the voltage range that our experimental setup could supply, the induced birefringence was almost proportional to E^2 . Thus, the Kerr law was valid in this voltage range and the slope represented the Kerr constant. The magnitude of K for sample 1-10 was $K = 5.87 \times 10^{-10} \text{ mV}^{-2}$.

Crystal polymorphism

Of the materials studied herein, compounds 1-10, 1-12, and 1-14 exhibited crystal polymorphism during the heating cycle. Compound 1-10 underwent a transition from crystal 1 (Cr_1) to crystal 2 (Cr_2) upon heating at a temperature of around 110.0°C . The optical micrographs of the change in Cr_1 to Cr_2 state are presented in Figure 8h–j. The SAXS/WAXS measurements of compound 1-10 at two different temperatures confirmed the presence of crystal polymorphism in the heating cycle. The intensity versus 2θ plot revealed the difference in peak position and peak nature recorded at two different temperatures, 100 and 120°C , for Cr_1 and Cr_2 , respectively (Figure 8a). The 2D diffractograms also substantiated the formation of two different crystal polymorphs. Interestingly, we have also observed morphological changes in compound 1-10 upon annealing at a temperature of 117°C , as verified by FESEM (field emission scanning electron microscopy) (Figure 8f,g). The color of the compound changed from bright yellow at room temperature (pristine compound) to whitish-yellow after heating to 117°C (Figure 8b,d). The color change was also observed in the two samples under UV light (Figure 8c,e). This whitish-yellow color of the compound remained stable for several hours. Details of crystal polymorphism of 1-12 and 1-14 are summarized in Figures S41, S42, S70, S72, and S74 in the Supporting Information.

Mechanochromism

Materials containing the cholesterol and salicylideneaniline moieties can be potentially used as mechanochromic materials. The study presented herein exploits the chiral bent-shaped materials for mechanochromic properties. All compounds of the homologous series were weakly fluorescent in solution (Figure S32 in the Supporting Information for the representative compound 1-14) and exhibited strong photoluminescence in the solid state. Upon applying mechanical energy through grinding, the visible color of compound 1-10 (as a representative case) changed from bright yellow to dark orange–green, as depicted in Figure 9a. Compound 1-10 also became amorphous and sticky upon grinding. The color change obtained upon grinding was reversible after the dropwise addition of dichloromethane to the well-ground sample (Figure 9a). Mechanochromic photoluminescent properties were confirmed by means of solid-state UV (in reflectance mode with KBr; Figure 9b) for representative compound 1-10. The π – π^* band in the neat state absorbed at a wavelength of $\lambda = 375 \text{ nm}$. However, upon mechanical grinding, the π – π^* band shifted to a

lower wavelength of 357 nm . The emission spectrum for 1-10 displayed a red shift as λ_{em} shifted from $\lambda = 533$ to 542 nm upon grinding the sample and the band returned to its original position after the addition of DCM (Figure 9d). Powder X-ray diffraction (PXRD) analysis showed that the material obtained after grinding was different from the neat sample because the crystallinity of the compound after grinding was reduced. The peaks in the ground sample were less sharp than those in the neat sample (Figure 9c). FESEM studies further confirmed the formation of a different sample after grinding. FESEM images obtained before grinding were different from the SEM images after grinding. The FESEM image of the neat sample had long fibers/rod-like structures (Figure 9f). However, upon mechanical grinding, it formed a sponge-like structure with a different stacking mode (Figure 9g). The schematic representation in Figure 9e elaborates the breaking of intermolecular interactions without breaking any covalent bonds.

Thermochromism

Thermochromism is the ability of the material to change color as the temperature is varied. The pitch of the CLCs is in the order of the wavelength of light ($\lambda = 400$ – 700 nm). Therefore, CLCs can undergo Bragg scattering and a change in temperature leads to a change in layer spacing. Hence, the color variation observed is due to a change in pitch ($\lambda = nP$, in which n is the average refractive index of the LC material and P is the pitch length of the helical structure).^[2] In this context, the effect of the phase transition of CLC materials cannot be ignored and combine with the effect of pitch length variation of the material to result in the observed thermochromism. CLCs are widely considered as thermochromic materials that find various applications, such as in a liquid-crystalline thermometer, thermography in medicine, and various branches of engineering. In general, thermotropic CLCs are viewed against a black background because the selective reflection caused by CLCs can be effectively seen upon it. In the present study, compound 1-10, exhibiting the N_{cyb}^* phase, showed thermochromic behavior upon cooling the sample.^[47,68]

The sample melted at a temperature of 145.4°C and a yellow liquid was formed (Figure 10a). Upon cooling and subsequently holding sample 1-10 at 125.0°C , the melted yellow sample started to convert into green at one of the corners (Figure 10b) because it converted to the N^* phase from the yellow liquid. Subsequent cooling to 120°C resulted in a green color that spread over a larger area (Figure 10c). At 115°C , the green color covered the entire sample (Figure 10d,e). Furthermore, at 110°C , the greenish color of the sample started to change to yellow. At 105°C , most of the sample turned yellow with a few greenish lines along the edge (Figure 10f). This conversion of green to yellow at 105°C could be rationalized due to crystallization of the sample. Upon further cooling to 100 and 90°C , the yellow color spread all over the sample due to complete crystallization of the sample and it persisted down to room temperature (Figure 10g,h). The schematic illustration in Figure 10i demonstrates the increase in pitch length with a decrease in temperature.

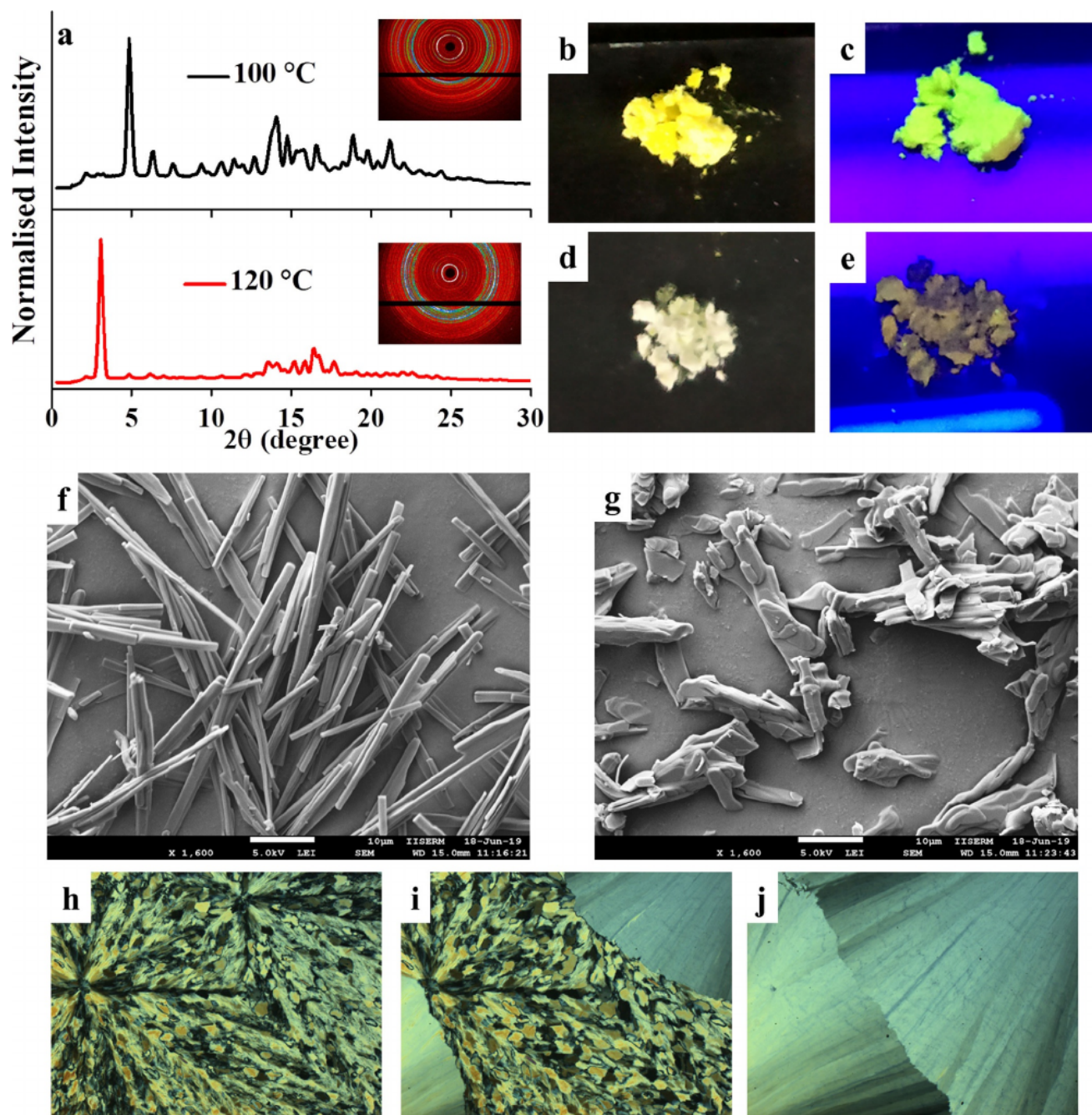


Figure 8. a) X-ray plot of two different crystal polymorphs of 1-10 at 100 °C (Cr_1 , black) and 120 °C (Cr_2 , red) along with their 2D images. b) Compound 1-10 in its pristine state in normal daylight. c) Compound 1-10 under UV light in its pristine state. d) Compound 1-10 upon thermal annealing at 117 °C in normal daylight. e) Thermally annealed compound 1-10 at 117 °C under UV light, (f,g) FESEM images of pristine compound 1-10 and after annealing at 117 °C respectively; POM micrographs of compound 1-10 showing (h) crystal 1 (Cr_1) at 107.7 °C (i) coexistence of Cr_1 and Cr_2 at 116.8 °C (a broad peak in the transition from Cr_1 to Cr_2 and a slight change in the temperature observed by DSC and POM, respectively), (j) Cr_2 at 121.8 °C.

Conclusion

We have successfully engineered a chiral BCLC, in which an electronegative chloro moiety was introduced at the transverse position of the central benzene ring. Previously, we had placed a methyl group at the same kink position of the molecular architecture and observed exotic BPIII, BPII/I, N_{Cyb}^* , TGBA, $SmAP_{Ar}$, SmA, and SmX phases (Figure 1a).^[47] Herein, the compounds

with a chloro core (Figure 1b) showed a cubic BP over a wide range of 16.4 °C; this is one of the few reports on a single-component BCLC compound. In addition, two homologues (1-12 and 1-14) exhibited an exotic phase sequence consisting of BPI/II, N^* , TGBA, SmA, and SmX; these are similar to those phases reported previously.^[47] Comparative DFT studies of the two types of molecules (one with a chloro core, compound 1-4 (Figure 1b), and another with a methyl core (Figure 1a)) sug-

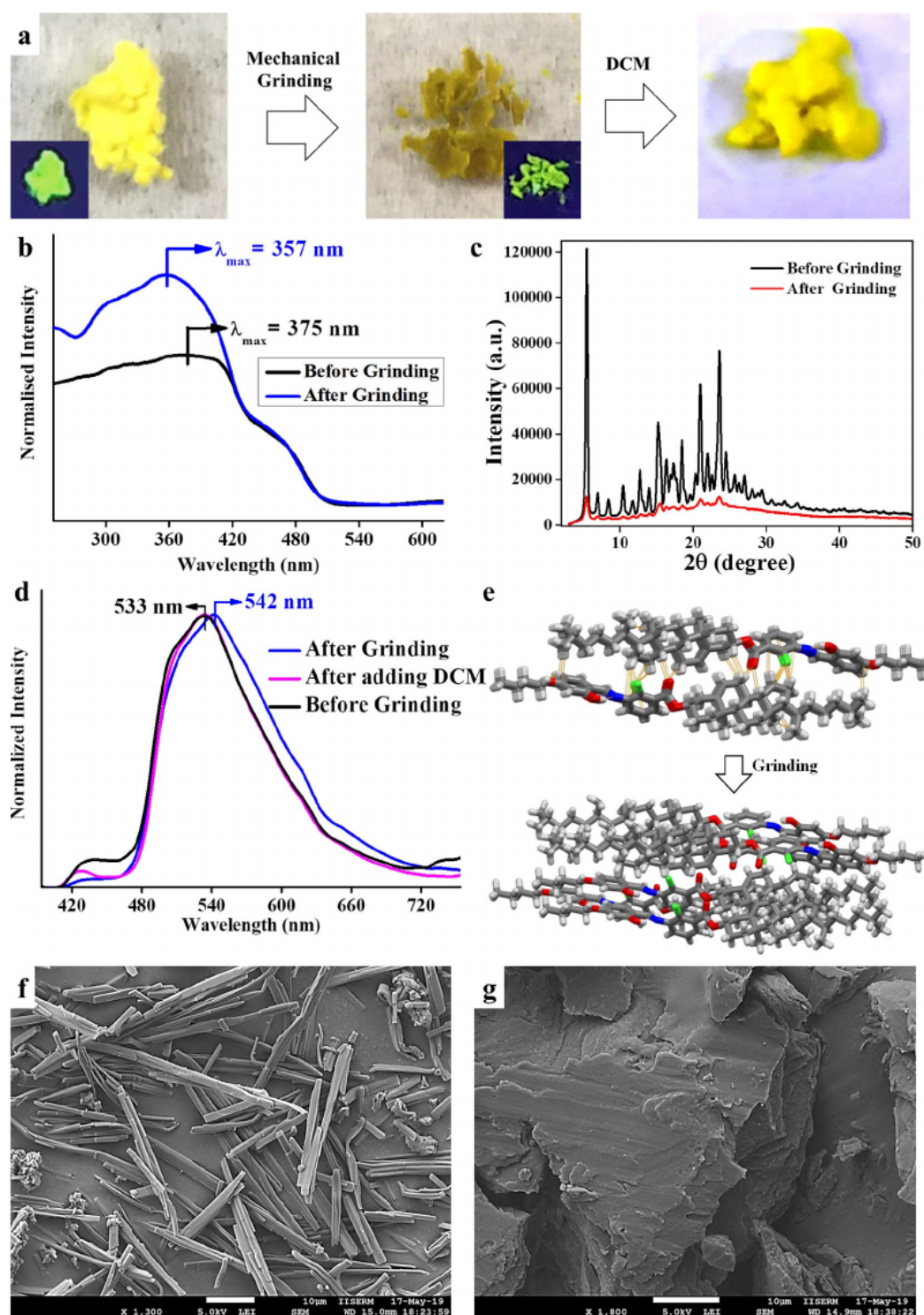


Figure 9. a) Images of compound 1-10 showing the change in color upon mechanical shearing and the reversibility of color change after the addition of dichloromethane (DCM); inset showing the images under UV light ($\lambda = 365$ nm). b) Absorption spectra of 1-10 in the solid state: the black line indicates the spectrum before grinding; the blue line indicates the spectrum after grinding. c) Intensity versus 2θ plot of 1-10 showing the change in the XRD pattern before and after mechanical grinding. d) Emission spectra of 1-10 in the solid state: the black line indicates the spectrum before grinding; the blue line indicates the spectrum after grinding; the pink line indicates the spectrum after the addition of DCM, $\lambda_{\text{ex}} = 375$ nm. e) Schematic illustration of the molecular arrangement before and after grinding, showing the change in weak molecular interactions. FESEM images of 1-10 before (f) and after (g) grinding.

gested an increased dipole moment along the transverse direction (due to the $-I$ effect of the $-\text{Cl}$ group), which immensely helped to stabilize the long-range cubic BP. Basically, the

chloro substituent makes the central core electron deficient relative to that of the methyl core. SCXRD analysis confirmed the bent architecture of the molecule and revealed fundamen-

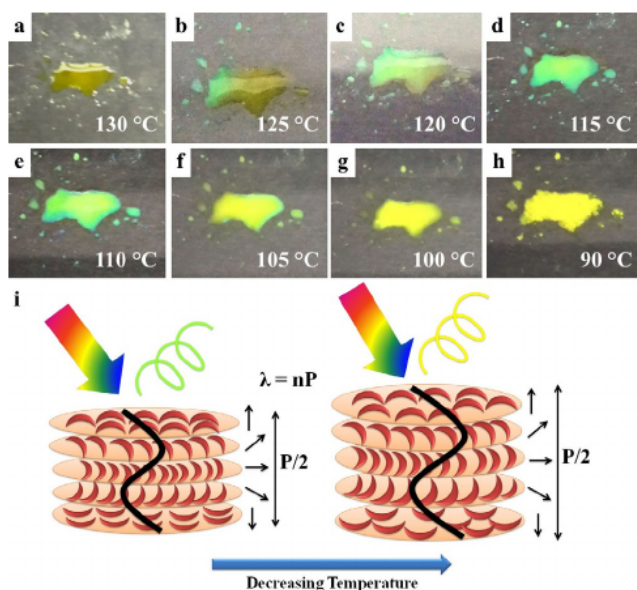


Figure 10. Photographs displaying the thermochromic behavior of 1-10 during cooling from an isotropic liquid (a), the transition to the mesophase (b,c), the mesophase (d,e), the transition to a crystal (f); the yellow color surrounded by the green line, and the crystal (g,h). i) A schematic illustration of the change in pitch and visible color of CLC with decreasing temperature.

tal structural insights, regarding the presence of two different types of conformers in an asymmetric unit, and their different weak intra- and intermolecular interactions, such as $\text{CH}\cdots\pi$ and $\text{CCl}\cdots\pi$ interactions. These weak interactions are of immense importance to unravel many fundamental aspects of structural biology and chemistry. The compounds exhibited multistimuli-responsive properties of polymorphism, mechanochromism, and thermochromism. The thermochromic behavior was excellent, showing a color change as a function of temperature, and the color at every temperature interval was extremely stable (in terms of several minutes).

Experimental Section

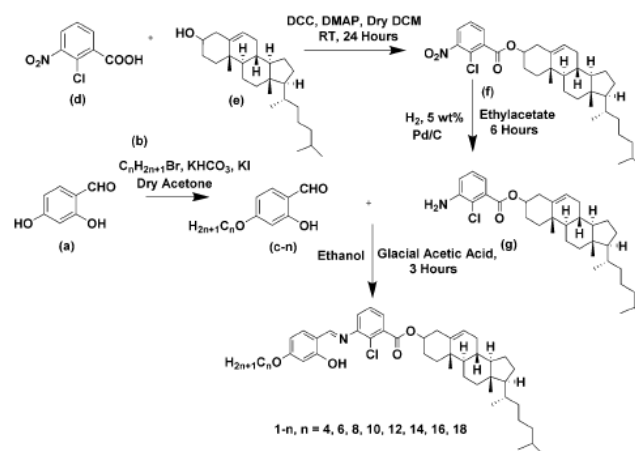
General

Details of the characterization techniques have been published elsewhere.^[47,60] Briefly, the instrumental details are as follows. Structural characterization of the compound was performed through a combination of ^1H and ^{13}C NMR spectroscopy (Bruker Biospin Switzerland Avance III 400 MHz). NMR spectra were recorded as solutions in deuterated chloroform, with tetramethylsilane (TMS) as an internal standard. Attenuated total reflectance (ATR; FTIR Bruker-ALPHA Bruker-1227-3513), UV/Vis/near-IR spectrophotometry (Labindia UV/Vis spectrophotometer 3000+), spectrofluorophotometry (Shimadzu, RF-6000), and mass spectrometry (Waters synapt g2s) were also used. FESEM was performed by using a JEOL JSM-7600F instrument. Mesomorphic studies were performed through POM, DSC, and SAXS/WAXS measurements. POM textural observations of the mesophase were performed with a Nikon Eclipse LV100POL polarizing microscope equipped with a Linkam heating stage (LTS 420). DSC measurements were performed on a PerkinElmer DSC 8000 instrument coupled to a controlled liquid nitrogen accessory (CLN 2) at a scan rate of $10^\circ\text{C min}^{-1}$. All images were captured by using a Q-imaging camera. XRD studies were per-

formed on the samples by using $\text{Cu}_{\text{K}\alpha}$ ($\lambda = 1.54 \text{ \AA}$) radiation from a GeniX3D microsource, with a Pilatus 200 K detector in the Xeuss 2.0 SAXS/WAXS system. Single-crystal XRD data were collected by using a Rigaku XtaLABmini X-ray diffractometer equipped with a mercury charge-coupled device (CCD) detector. Graphite monochromated $\text{Mo}_{\text{K}\alpha}$ radiation ($\lambda = 0.71073 \text{ \AA}$) at room temperature with ω scans was used, and the space group determination was performed by using Olex2.

General procedure for synthesis of 1-*n*

Scheme 1 provides the route for preparing the desired bent-shaped LCs. The final compounds were prepared by heating a solution of *c-n* (4-*n*-alkoxy-2-hydroxybenzaldehyde, 1 equiv) with compound **g** (1 equiv) at reflux in ethanol with a few drops of glacial acetic acid as a catalyst for 3 h. The precipitated product was purified by repeated recrystallization from absolute ethanol. The final product was obtained as a light yellow solid.^[47]



Scheme 1. Schematic route for the preparation of the desired bent-shaped LCs. DCC = *N,N*-dicyclohexylcarbodiimide, DMAP = 4-dimethylaminopyridine.

Compound 1-4

Yield: 85%; ^1H NMR (400 MHz, CDCl_3): $\delta = 13.49$ (s, 1H; $-\text{OH}$), 8.49 (s, 1H; $-\text{CH}=\text{N}-$), 7.56 (dt, $J = 7.4, 1.6$ Hz, 1H; Ar-H), 7.36–7.27 (m, 3H; Ar-H), 6.51–6.48 (m, 2H; Ar-H), 5.44 (d, $J = 5.0$ Hz, 1H; $-\text{CH}=\text{C}-$ in cholesteryl), 4.95–4.87 (m, 1H; $-\text{CH}-\text{O}-$ in cholesteryl), 4.01 (t, $J = 8$ Hz, 2H; $-\text{OCH}_2-$), 2.52–2.44 (m, 2H; $-\text{CH}_2-$ in cholesteryl), 2.06–0.85 (m, 45H; extensive coupling in cholesteryl), 0.68 ppm (s, 3H; $-\text{CH}_3$ in cholesteryl); ^{13}C NMR (100 MHz, CDCl_3): $\delta = 11.9, 13.9, 18.7, 19.2, 19.4, 21.1, 22.6, 22.9, 23.9, 24.3, 27.8, 28.1, 28.3, 31.1, 31.9, 32.0, 35.8, 36.2, 36.7, 37.0, 38.1, 39.5, 39.7, 42.3, 50.0, 56.1, 56.7, 68.0, 75.8, 101.6, 108.0, 112.8, 121.6, 123.0, 127.2, 127.7, 127.8, 133.1, 133.9, 139.5, 147.0, 162.9, 164.0, 164.2, 165.6$ ppm; ATR: 2867–2930 (intramolecular H-bond of $\text{O}-\text{H}\cdots\text{N}$), 1734 ($\text{C}=\text{O}$ stretching of ester), 1612 cm^{-1} ($\text{CH}=\text{N}$ stretching of imine); UV/Vis: $\lambda = 278, 334$ nm; HRMS (ESI-MS): m/z calcd for $\text{C}_{45}\text{H}_{62}\text{ClNO}_4$ [$M+\text{H}$] $^+$: 716.4445; found: 716.4409.

Compound 1-6

Yield: 82%; ^1H NMR (400 MHz, CDCl_3): $\delta = 13.48$ (s, 1H; $-\text{OH}$), 8.50 (s, 1H; $-\text{CH}=\text{N}-$), 7.57 (dd, $J = 7.4$ Hz, 1.8 Hz, 1H; Ar-H), 7.37–7.28 (m, 3H; Ar-H), 6.52–6.49 (m, 2H; Ar-H), 5.44 (d, $J = 5.1$ Hz, 1H; $-\text{CH}=\text{C}-$ in cholesteryl), 4.95–4.87 (m, 1H; $-\text{CH}-\text{O}-$ in cholesteryl), 4.01 (t, $J = 4, 8$ Hz, 2H; $-\text{OCH}_2-$), 2.51–2.44 (m, 2H; $-\text{CH}_2-$ in cho-

lesteryl), 2.03–0.86 (m, 49H; extensive coupling in cholesteryl), 0.69 ppm (s, 3H; –CH₃ in cholesteryl); ¹³C NMR (100 MHz, CDCl₃): δ = 11.9, 14.1, 18.7, 19.4, 21.1, 22.60, 22.62, 22.9, 23.9, 24.3, 25.7, 27.8, 28.0, 28.3, 29.0, 31.6, 31.9, 32.0, 35.8, 36.2, 36.7, 37.0, 38.0, 39.5, 39.7, 42.3, 50.0, 56.1, 56.7, 68.3, 75.7, 101.6, 108.0, 112.8, 121.6, 123.0, 127.2, 127.7, 127.8, 133.1, 133.9, 139.5, 147.0, 162.8, 164.0, 164.2, 165.6 ppm; ATR: 2850–2950 (intramolecular H-bond of O–H⋯N), 1725 (C=O stretching of ester), 1619 cm⁻¹ (CH=N stretching of imine); UV/Vis: λ = 278, 334 nm; HRMS (ESI-MS): *m/z* calcd for C₄₇H₆₆ClNO₄ [M+H]⁺: 744.4758; found: 744.4728.

Compound 1-8

Yield: 83%; ¹H NMR (400 MHz, CDCl₃): δ = 13.48 (s, 1H; –OH), 8.50 (s, 1H; –CH=N–), 7.57 (dt, *J* = 7.4, 1.6 Hz, 1H; Ar–H), 7.37–7.27 (m, 3H; Ar–H), 6.52–6.49 (m, 2H; Ar–H), 5.44 (d, *J* = 4.7 Hz, 1H; –CH=C– in cholesteryl), 4.94–4.88 (m, 1H; –CH–O– in cholesteryl), 4.00 (t, *J* = 8, 4 Hz, 2H; –OCH₂–), 2.50–2.44 (m, 2H; –CH₂– in cholesteryl), 2.04–0.87 (m, 53H; extensive coupling in cholesteryl), 0.68 ppm (s, 3H; –CH₃ in cholesteryl); ¹³C NMR (100 MHz, CDCl₃): δ = 11.9, 14.1, 18.7, 19.4, 21.1, 22.6, 22.7, 22.9, 23.9, 24.3, 26.0, 27.8, 28.1, 28.3, 29.1, 29.3, 29.3, 31.8, 31.9, 32.0, 35.8, 36.2, 36.7, 37.0, 38.1, 39.5, 39.7, 42.3, 50.0, 56.1, 56.7, 68.4, 75.8, 101.6, 108.0, 112.8, 121.6, 123.0, 127.2, 127.7, 127.8, 133.2, 133.9, 139.5, 147.0, 162.9, 164.0, 164.2, 165.6 ppm; ATR: 2837–2950 (intramolecular H-bond of O–H⋯N), 1736 (C=O stretching of ester), 1611 cm⁻¹ (CH=N stretching of imine); UV/Vis: λ = 278, 334 nm; HRMS (ESI-MS): *m/z* calcd for C₄₉H₇₀ClNO₄ [M+H]⁺: 772.5071; found: 772.5041.

Compound 1-10

Yield: 84%; ¹H NMR (400 MHz, CDCl₃): δ = 13.48 (s, 1H; –OH), 8.50 (s, 1H; –CH=N–), 7.57 (dd, *J* = 7.5 Hz, 1.8 Hz, 1H; Ar–H), 7.37–7.28 (m, 3H; Ar–H), 6.52–6.49 (m, 2H; Ar–H), 5.44 (d, *J* = 5.1 Hz, 1H; –CH=C– in cholesteryl), 4.95–4.87 (m, 1H; –CH–O– in cholesteryl), 4.01 (t, *J* = 4, 8 Hz, 2H; –OCH₂–), 2.51–2.49 (m, 2H; –CH₂– in cholesteryl), 2.03–0.86 (57H; extensive coupling in cholesteryl), 0.69 ppm (s, 3H; –CH₃ in cholesteryl); ¹³C NMR (100 MHz, CDCl₃): δ = 11.9, 14.2, 18.7, 19.4, 21.1, 22.6, 22.7, 22.9, 23.9, 24.3, 26.0, 27.8, 28.0, 28.3, 29.1, 29.35, 29.39, 29.6, 31.87, 31.92, 31.95, 35.8, 36.2, 36.7, 37.0, 38.0, 39.5, 39.7, 42.3, 50.0, 56.1, 56.7, 68.4, 75.7, 101.6, 108.0, 112.8, 121.5, 123.0, 127.2, 127.7, 127.8, 133.1, 133.9, 139.5, 147.0, 162.8, 164.0, 164.2, 165.6 ppm; ATR: 2824–2943 (intramolecular H-bond of O–H⋯N), 1711 (C=O stretching of ester), 1605 cm⁻¹ (CH=N stretching of imine); UV/Vis: λ = 278, 334 nm; HRMS (ESI-MS): *m/z* calcd for C₅₁H₇₄ClNO₄ [M+H]⁺: 800.5384; found: 800.5345.

Compound 1-12

Yield: 85%; ¹H NMR (400 MHz, CDCl₃): δ = 13.47 (s, 1H; –OH), 8.50 (s, 1H; –CH=N–), 7.57 (dd, *J* = 7.5, 1.8 Hz, 1H; Ar–H), 7.36–7.27 (m, 3H; Ar–H), 6.52–6.49 (m, 2H; Ar–H), 5.44 (d, *J* = 5.0 Hz, 1H; –CH=C– in cholesteryl), 4.93–4.87 (m, 1H; –CH–O– in cholesteryl), 4.01 (t, *J* = 4, 8 Hz, 2H; –OCH₂–), 2.51–2.49 (m, 2H; –CH₂– in cholesteryl), 2.03–0.86 (m, 61H; extensive coupling in cholesteryl), 0.69 ppm (s, 3H; –CH₃ in cholesteryl); ¹³C NMR (100 MHz, CDCl₃): δ = 11.9, 14.2, 18.7, 19.4, 21.1, 22.6, 22.7, 22.9, 23.9, 24.3, 26.0, 27.8, 28.0, 28.3, 29.1, 29.4, 29.59, 29.62, 29.66, 29.69, 31.9, 32.0, 35.8, 36.2, 36.7, 37.0, 38.1, 39.5, 39.7, 42.3, 50.0, 56.1, 56.7, 68.4, 75.8, 101.6, 108.0, 112.8, 121.6, 123.0, 127.2, 127.7, 127.8, 133.2, 133.9, 139.5, 147.0, 162.9, 164.0, 164.2, 165.6 ppm; ATR: 2849–2940 (intramolecular H-bond of O–H⋯N), 1715 (C=O stretching of ester), 1605 cm⁻¹ (CH=N stretching of imine); UV/Vis: λ = 278, 334 nm; HRMS (ESI-MS): *m/z* calcd for C₅₃H₇₈ClNO₄ [M+H]⁺: 828.5697; found: 828.5660.

Compound 1-14

Yield: 81%; ¹H NMR (400 MHz, CDCl₃): δ = 13.49 (s, 1H; –OH), 8.49 (s, 1H; –CH=N–), 7.56 (dd, *J* = 7.4 Hz, 1.8 Hz, 1H; Ar–H), 7.36–7.27 (m, 3H; Ar–H), 6.51–6.48 (m, 2H; Ar–H), 5.44 (d, *J* = 4.7 Hz, 1H; –CH=C– in cholesteryl), 4.95–4.87 (m, 1H; –CH–O– in cholesteryl), 4.00 (t, *J* = 8 Hz, 2H; –OCH₂–), 2.52–2.44 (m, 2H; –CH₂– in cholesteryl), 2.06–0.86 (m, 65H; extensive coupling in cholesteryl), 0.69 ppm (s, 3H; –CH₃ in cholesteryl); ¹³C NMR (100 MHz, CDCl₃): δ = 11.9, 14.2, 18.7, 19.4, 21.1, 22.6, 22.7, 22.9, 23.9, 24.3, 26.0, 27.8, 28.0, 28.3, 29.1, 29.4, 29.58, 29.62, 29.65, 29.69, 29.71, 29.73, 31.9, 32.0, 35.8, 36.2, 36.7, 37.0, 38.0, 39.5, 39.7, 42.3, 50.0, 56.1, 56.7, 68.4, 75.7, 101.6, 108.0, 112.8, 121.5, 123.0, 127.2, 127.7, 127.8, 133.1, 133.9, 139.5, 147.0, 162.8, 164.0, 164.2, 165.6 ppm; ATR: 2847–2945 (intramolecular H-bond of O–H⋯N), 1715 (C=O stretching of ester), 1605 cm⁻¹ (CH=N stretching of imine); UV/Vis: λ = 278, 334 nm; HRMS (ESI-MS): *m/z* calcd for C₅₅H₈₂ClNO₄ [M+H]⁺: 856.6010; found: 856.5967.

Compound 1-16

Yield: 87%; ¹H NMR (400 MHz, CDCl₃): δ = 13.48 (s, 1H; –OH), 8.49 (s, 1H; –CH=N–), 7.56 (dt, *J* = 7.3, 1.4 Hz, 1H; Ar–H), 7.36–7.27 (m, 3H; Ar–H), 6.51–6.48 (m, 2H; Ar–H), 5.44 (d, *J* = 5.0 Hz, 1H; –CH=C– in cholesteryl), 4.95–4.87 (m, 1H; –CH–O– in cholesteryl), 4.00 (t, *J* = 8 Hz, 2H; –OCH₂–), 2.52–2.47 (m, 2H; –CH₂– in cholesteryl), 2.06–0.86 (m, 69H; extensive coupling in cholesteryl), 0.69 ppm (s, 3H; –CH₃ in cholesteryl); ¹³C NMR (100 MHz, CDCl₃): δ = 11.9, 14.2, 18.7, 19.4, 21.1, 22.6, 22.7, 22.9, 23.9, 24.3, 26.0, 27.8, 28.1, 28.3, 29.1, 29.4, 29.6, 29.63, 29.69, 29.71, 29.73, 31.9, 32.0, 35.8, 36.2, 36.7, 37.0, 38.1, 39.5, 39.7, 42.3, 50.0, 56.1, 56.7, 68.4, 75.8, 101.6, 108.0, 112.8, 121.6, 123.0, 127.2, 127.7, 127.8, 133.2, 133.9, 139.5, 147.0, 162.9, 164.0, 164.2, 165.6 ppm; ATR: 2850–2920 (intramolecular H-bond of O–H⋯N), 1717 (C=O stretching band of ester), 1615 cm⁻¹ (CH=N stretching of imine); UV/Vis: λ = 278, 334 nm; HRMS (ESI-MS): *m/z* calcd for C₅₇H₈₆ClNO₄ [M+H]⁺: 884.6323; found: 884.6349.

Compound 1-18

Yield: 85%; ¹H NMR (400 MHz, CDCl₃): δ = 13.47 (s, 1H; –OH), 8.50 (s, 1H; –CH=N–), 7.57 (d, *J* = 7.2 Hz, 1H; Ar–H), 7.37–7.27 (m, 3H; Ar–H), 6.52–6.49 (m, 2H; Ar–H), 5.44 (d, *J* = 3.4 Hz, 1H; –CH=C– in cholesteryl), 4.94–4.87 (m, 1H; –CH–O– in cholesteryl), 4.00 (t, *J* = 8, 4 Hz, 2H; –OCH₂–), 2.51–2.49 (m, 2H; –CH₂– in cholesteryl), 2.03–0.86 (m, 73H; extensive coupling in cholesteryl), 0.69 ppm (s, 3H; –CH₃ in cholesteryl); ¹³C NMR (100 MHz, CDCl₃): δ = 11.9, 14.2, 18.7, 19.4, 21.1, 22.6, 22.7, 22.9, 23.9, 24.3, 26.0, 27.8, 28.1, 28.3, 29.1, 29.4, 29.59, 29.63, 29.69, 29.73, 31.9, 32.0, 35.8, 36.2, 36.7, 37.0, 38.1, 39.5, 39.7, 42.3, 50.0, 56.1, 56.7, 68.4, 75.8, 101.6, 108.0, 112.8, 121.6, 123.0, 127.2, 127.7, 127.8, 133.2, 133.9, 139.5, 147.0, 162.9, 164.0, 164.2, 165.6 ppm; ATR: 2849–2915 (intramolecular H-bond of O–H⋯N), 1714 (C=O stretching of ester), 1607 cm⁻¹ (CH=N stretching of imine); UV/Vis: λ = 278, 334 nm; HRMS (ESI-MS): *m/z* calcd for C₅₉H₉₀ClNO₄ [M+H]⁺: 912.6636; found: 912.6690.

Acknowledgements

IISER Mohali is acknowledged for the SAXS/WAXS, NMR, FESEM and departmental single-crystal diffractometer. V.P. and S.K. acknowledge IISER Mohali for PhD fellowships. G.M. acknowledges DST-SERB, India, for a National Post-Doctoral Fellowship (NPDF/2016/000560) and Prof. N. V. S. Rao. S.K.P. acknowledges

CSIR Project File No. 02(0311)/17/EMR-II and SERB Project File No. (CRG/2019/000901/OC).

Conflict of interest

The authors declare no conflict of interest.

Keywords: liquid crystals • mechanochromism • phase transitions • single crystals • thermochromism

- [1] I. Agranat, H. Caner, J. Caldwell, *Nat. Rev.* **2002**, *1*, 753–768.
- [2] M. Mitov, *Soft Matter* **2017**, *13*, 4176–4209.
- [3] N. Tamaoki, *Adv. Mater.* **2001**, *13*, 1135–1147.
- [4] H. Wang, H. K. Bisoyi, A. M. Urbas, T. J. Bunning, Q. Li, *J. Am. Chem. Soc.* **2019**, *141*, 8078–8082.
- [5] H. Khandelwal, E. P. A. van Heeswijk, A. P. H. J. Schenning, M. G. Debije, *J. Mater. Chem. C* **2019**, *7*, 7395–7398.
- [6] J. W. Goodby, *Proc. R. Soc. London Ser. A* **2012**, *468*, 1521–1542.
- [7] T. C. Lubensky, A. B. Harris, R. D. Kamien, G. Yan, *Ferroelectrics* **1998**, *212*, 1–20.
- [8] H. J. Coles, M. N. Pivnenko, *Nature* **2005**, *436*, 997–1000.
- [9] M. Nakata, Y. Takanishi, J. Watanabe, H. Takezoe, *Phys. Rev. E* **2003**, *68*, 041710.
- [10] R. K. Khan, S. T. urlapati, N. V. S. Rao, R. Pratibha, W. Drzewinski, R. Dabrowski, S. Ghosh, *J. Mater. Chem. C* **2017**, *5*, 6729–6737.
- [11] Y. Hisakado, H. Kikuchi, T. Nagamura, T. Kajiyama, *Adv. Mater.* **2005**, *17*, 96–98.
- [12] H. Kikuchi, M. Yokota, Y. Hisakado, H. Yang, T. Kajikawa, *Nat. Mater.* **2002**, *1*, 64–68.
- [13] S. Yokoyama, S. Mashiko, H. Kikuchi, K. Uchida, T. Nagamura, *Adv. Mater.* **2006**, *18*, 48–51.
- [14] S. R. Renn, T. C. Lubensky, *Phys. Rev. A* **1988**, *38*, 2132–2147.
- [15] J. W. Goodby, M. A. Waugh, S. M. Stein, E. Chin, R. Pindak, J. S. Patel, *Nature* **1989**, *337*, 449–452.
- [16] J. W. Goodby, M. A. Waugh, S. M. Stein, E. Chin, R. Pindak, J. S. Patel, *J. Am. Chem. Soc.* **1989**, *111*, 8119–8125.
- [17] C. C. Huang, D. S. Lin, J. W. Goodby, M. A. Waugh, S. M. Stein, E. Chin, *Phys. Rev. A* **1989**, *40*, 4153–4156.
- [18] A. J. Slaney, J. W. Goodby, *J. Mater. Chem.* **1991**, *1*, 5–10.
- [19] A. J. Slaney, J. W. Goodby, *Liq. Cryst.* **1991**, *9*, 849–861.
- [20] A. Bouchta, H. T. Nguyen, M. F. Achard, F. Hardouin, C. Destrade, *Liq. Cryst.* **1992**, *12*, 575–591.
- [21] P. G. de Gennes, *Solid State Commun.* **1972**, *10*, 753–756.
- [22] A. Jáklí, O. D. Lavrentovich, J. V. Selinger, *Rev. Mod. Phys.* **2018**, *90*, 045004 (1–68).
- [23] S. Kumar, A. N. Gowda, *Liq. Cryst. Rev.* **2015**, *3*, 99–145.
- [24] R. A. Reddy, C. Tschierske, *J. Mater. Chem.* **2006**, *16*, 907–961.
- [25] J. Etxebarria, M. B. Ros, *J. Mater. Chem.* **2008**, *18*, 2919–2926.
- [26] G. Pelzl, S. Diele, W. Weissflog, *Adv. Mater.* **1999**, *11*, 707–724.
- [27] C. Tschierske, G. Dantlgraber, *Pramana* **2003**, *61*, 455–481.
- [28] M. B. Ros, J. L. Serrano, M. R. de la Fuente, C. L. Folcia, *J. Mater. Chem.* **2005**, *15*, 5093–5098.
- [29] H. Takezoe, Y. Takanishi, *Jpn. J. Appl. Phys.* **2006**, *45*, 597–625.
- [30] W. Weissflog, H. N. Sheenivasa Murthy, S. Diele, G. Pelzl, *Philos. Trans. R. Soc. London Ser. A* **2006**, *364*, 2657–2679.
- [31] H. F. Gleeson, S. Kaur, V. Görtz, A. Belaïssaoui, S. Cowling, J. W. Goodby, *ChemPhysChem* **2014**, *15*, 1251–1260.
- [32] S.-T. Hur, M.-G. Gim, H.-J. Yoo, S.-W. Choi, H. Takezoe, *Soft Matter* **2011**, *7*, 8800–8803.
- [33] I.-H. Chiang, C.-J. Long, H.-C. Lin, W.-T. Chuang, J.-J. Lee, H.-C. Lin, *ACS Appl. Mater. Interfaces* **2014**, *6*, 228–235.
- [34] K. V. Le, M. Hafuri, H. Ocak, B. Bilgin-Eran, C. Tschierske, T. Sasaki, F. Araoka, *ChemPhysChem* **2016**, *17*, 1425–1429.
- [35] C. V. Yelamaggad, I. S. Shashikala, G. Liao, D. S. S. Rao, S. K. Prasad, Q. Li, A. Jáklí, *Chem. Mater.* **2006**, *18*, 6100–6102.
- [36] H. Ocak, B. Bilgin-Eran, D. Guzeller, M. Prehm, C. Tschierske, *Chem. Commun.* **2015**, *51*, 7512–7515.
- [37] R. A. Reddy, B. K. Sadashiva, U. Baumeister, *J. Mater. Chem.* **2005**, *15*, 3303–3316.
- [38] H. Ocak, B. Bilgin-Eran, M. Prehm, S. Schymura, J. P. F. Lagerwall, C. Tschierske, *Soft Matter* **2011**, *7*, 8266–8280.
- [39] Y. Sagara, T. Kato, *Nat. Chem.* **2009**, *1*, 605–610.
- [40] C. Calvino, L. Neumann, C. Weder, S. Schrettl, *J. Polym. Sci. Part A* **2017**, *55*, 640–652.
- [41] P. Shi, Y. Duan, W. Wei, Z. Xu, Z. Li, T. Han, *J. Mater. Chem. C* **2018**, *6*, 2476–2482.
- [42] Y. Sagara, S. Yamane, M. Mitani, C. Weder, T. Kato, *Adv. Mater.* **2016**, *28*, 1073–1095.
- [43] J.-W. Hu, H.-Y. Tsai, S.-K. Fang, C.-W. Chang, L.-C. Wang, K.-Y. Chen, *Dyes Pigm.* **2017**, *145*, 493–504.
- [44] P. Pallavi, V. Kumar, M. W. Hussain, A. Patra, *ACS Appl. Mater. Interfaces* **2018**, *10*, 44696–44705.
- [45] X. Liu, A. Li, W. Xu, Z. Ma, X. Jia, *Mater. Chem. Front.* **2019**, *3*, 620–625.
- [46] K. Miyagi, Y. Teramoto, *J. Mater. Chem. C* **2018**, *6*, 1370–1376.
- [47] V. Punjani, G. Mohiuddin, S. Kaur, R. K. Khan, S. Ghosh, S. K. Pal, *Chem. Commun.* **2018**, *54*, 3452–3455.
- [48] G. Mohiuddin, V. Punjani, S. K. Pal, *ChemPhysChem* **2015**, *16*, 2739–2744.
- [49] N. Begum, S. Turlapati, S. Debnath, G. Mohiuddin, D. D. Sarkar, N. V. S. Rao, *Liq. Cryst.* **2013**, *40*, 1105–1115.
- [50] K. Upadhyaya, V. Gude, G. Mohiuddin, N. V. S. Rao, *Beilstein J. Org. Chem.* **2013**, *9*, 26–35.
- [51] V. Jain, G. Mohiuddin, S. K. Pal, *J. Mol. Struct.* **2020**, *1202*, 127383.
- [52] S. Kaur, G. Mohiuddin, V. Punjani, R. K. Khan, S. Ghosh, S. K. Pal, *J. Mol. Liq.* **2019**, *295*, 111687.
- [53] N. Begum, S. Kaur, G. Mohiuddin, R. Nandi, S. P. Gupta, N. V. S. Rao, S. K. Pal, *J. Phys. Chem. B* **2019**, *123*, 4443–4451.
- [54] V. Gude, D. Rout, M. K. Panigrahi, K. Biradha, *Photochem. Photobiol. Sci.* **2018**, *17*, 1386–1395.
- [55] S. Kaur, V. Punjani, G. Mohiuddin, S. K. Pal, *New J. Chem.* **2017**, *41*, 5403–5411.
- [56] T. N. Ahipa, V. Kumar, D. S. S. Rao, S. K. Prasad, A. V. Adhikari, *CrystEngComm* **2014**, *16*, 5573–5582.
- [57] W. Weissflog, U. Baumeister, M.-G. Tamba, G. Pelzl, H. Kresse, R. Friedemann, G. Hempel, R. Kurz, M. Roos, K. Merzweiler, A. Jáklí, C. Zhang, N. Diorio, R. Stannarius, A. Eremine, U. Korneke, *Soft Matter* **2012**, *8*, 2671–2685.
- [58] D.-Y. Kim, P. Nayek, S. Kim, K. S. Ha, M. H. Jo, C.-H. Hsu, Y. Cao, S. Z. D. Cheng, S. H. Lee, K.-U. Jeong, *Cryst. Growth Des.* **2013**, *13*, 1309–1315.
- [59] I. Dierking, F. Gießelmann, P. Zugenmaier, *Liq. Cryst.* **1994**, *17*, 17–22.
- [60] S. Kaur, G. Mohiuddin, P. Satapathy, R. Nandi, V. Punjani, S. K. Prasad, S. K. Pal, *Mol. Syst. Des. Eng.* **2018**, *3*, 839–852.
- [61] G. Mohiuddin, N. Begum, N. V. S. Rao, S. Kaur, V. Punjani, R. K. Khan, S. Ghosh, S. K. Pal, *Liq. Cryst.* **2017**, *44*, 2247–2258.
- [62] P. Sathyanarayana, S. Radhika, B. K. Sadashiva, S. Dhara, *Soft Matter* **2012**, *8*, 2322–2327.
- [63] F. Gouda, K. Skarp, S. T. Lagerwall, *Ferroelectrics* **1991**, *113*, 165–206.
- [64] S. Al-Zangana, M. Iliut, G. Boran, M. Turner, A. Vijayaraghavan, I. Dierking, *Sci. Rep.* **2016**, *6*, 31885.
- [65] A. K. George, D. M. Potukuchia, S. H. Al-Harhi, C. Carboni, *Z. Naturforsch. A* **2004**, *59*, 659–664.
- [66] M. K. Das, B. Barman, B. Das, V. Hamplová, A. Bubnov, *Crystals* **2019**, *9*, 473.
- [67] R. Sahoo, J. Ananthaiah, R. Dabrowski, S. Dhara, *Phys. Rev. E* **2014**, *90*, 012506.
- [68] I. Sage, *Liq. Cryst.* **2011**, *38*, 1551–1561.

Manuscript received: December 18, 2019

Revised manuscript received: February 2, 2020

Accepted manuscript online: February 21, 2020

Version of record online: April 21, 2020